Letter

Complete mapping of the thermoelectric properties of a single molecule

Pascal Gehring, [1✉,2]

Email pascal.gehring@uclouvain.be

Jakub K. Sowa, [3,4]

Chunwei Hsu, [1]

Joeri de Bruijckere, [1]

Martijn van der Star, [1]

Jennifer J. Le Roy, [3]

Lapo Bogani, [3]

Erik M. Gauger, [5]

Herre S. J. van der Zant, [1]

[1] Kavli Institute of Nanoscience, Delft University of Technology, Delft, The Netherlands

[2] IMCN/NAPS, Université Catholique de Louvain, Louvain-la-Neuve, Belgium

[3] Department of Materials, University of Oxford, Oxford, United Kingdom

[4] Department of Chemistry, Northwestern University, Evanston, IL, USA

[5] SUPA, Institute of Photonics and Quantum Sciences, Heriot-Watt University, Edinburgh, UK

Received: 25 June 2020 / Accepted: 16 December 2020

Abstract

Theoretical studies suggest that mastering the thermocurrent through single molecules can lead to thermoelectric energy harvesters with unprecedentedly high efficiencies.[1, 2, 3, 4, 5, 6] This can be achieved by optimizing molecule length,[7] optimizing the tunnel coupling strength of molecules via chemical anchor groups[8] or by creating localized states in the backbone with resulting quantum interference features.[4] Empirical verification of these predictions, however, faces considerable experimental challenges and is still awaited. Here we use a novel measurement protocol that simultaneously probes the conductance and thermocurrent flow as a function of bias voltage and gate voltage. We find that the resulting thermocurrent is strongly asymmetric with respect to the gate voltage, with evidence of molecular excited states in the thermocurrent Coulomb diamond maps. These features can be reproduced by a rate-equation model only if it accounts for both the vibrational coupling and the electronic degeneracies, thus giving direct insight into the interplay of electronic and vibrational degrees of freedom, and the role of spin entropy in single molecules. Overall these results show that thermocurrent measurements can be used as a spectroscopic tool to access molecule-specific quantum transport phenomena.

Editor's Summary

A measurement protocol allows the conductance and the thermocurrent of a single molecule to be determined simultaneously.

Main

Intense theoretical scrutiny predicts that the interplay between the spin, vibrational and electronic degrees of freedom should result in high thermoelectric energy harvesting efficiencies,[1, 2, 3, 4, 5] in ways strongly linked to the molecular design. These theoretical predictions are difficult to test experimentally: they require accurate measurements of minute thermocurrent signals (in the femto- to picoamp range) in a single molecule with a tunable electrochemical potential[9, 10], and simultaneous control of temperature, T, bias and gate voltages, V_{sd} and V_{G}, and thermal bias, $\Delta\tilde{T}$, in a parameter space wide enough to access both the linear and non-linear regimes. Due to these difficulties, previous schemes typically relied on sequential measurements of the conductance G and the Seebeck coefficient S (refs. [2, 7, 8, 9, 10]) which can cause large errors in evaluating the power factor S^2G, because of molecular reconfiguration and drift in the measurement electronics.[10, 11] Methods that provide G and S simultaneously fundamentally prevent applying gate and bias voltages.[12] Full maps, in which electric currents and thermocurrents are thoroughly separated, are therefore currently unavailable.

We overcome these challenges by employing a measurement scheme that allows us to simultaneously record the complete bias V_{sd} and gate voltage V_{G} dependent conductance, G, and thermocurrent, $\tilde{I}_{\mathrm{th}}$, maps of a single-molecule junction. The devices consist of a gold molecular junction manufactured by electromigration and self-breaking[13] of the gold contacts (Methods) where d.c. and a.c. currents can be applied (Fig. 1a). Micro-heaters are fabricated in direct thermal contact with the source and drain leads. Here we use the [Gd(tpy-SH)$_2$(NCS)$_3$] complex (hereinafter Gd-tpy, synthesis in Supplementary Section 6), because the Gd(III) metal affords a high-spin magnetic centre (term symbol $^8\mathrm{S}_{7/2}$, spin $\Sigma = 7/2$), so that spin degrees of freedom can be studied in conjunction with charge and vibrational ones. Gd-tpy molecules were deposited by immersion in a solution after electromigration followed by self-breaking. A possible junction geometry with asymmetric coupling is depicted in Fig. 1b.

Fig. 1

The experimental system.

a, False-colour scanning electron microscopy image of the typical experimental junctions. The schematic circuit diagram indicates which the terminals are used to apply a gate voltage V_{G}, a d.c. bias voltage V_{sd}, an a.c. bias voltage $\tilde{V}_{\mathrm{sd}}(\omega_2)$ and an a.c. heater current $\tilde{I}_{\mathrm{h}}(\omega_1)$, and which terminals are used to measure a d.c. current I_{sd}, an a.c. current $\tilde{I}_{\mathrm{sd}}(\omega_2)$ and a thermocurrent $\tilde{I}_{\mathrm{th}}(2\omega_1)$. **b**, The structure of the Gd-tpy molecule (see also Supplementary Fig. 6) bridging the electrodes, as obtained by X-ray crystallography, depicted here as coupled asymmetrically to the two gold leads.

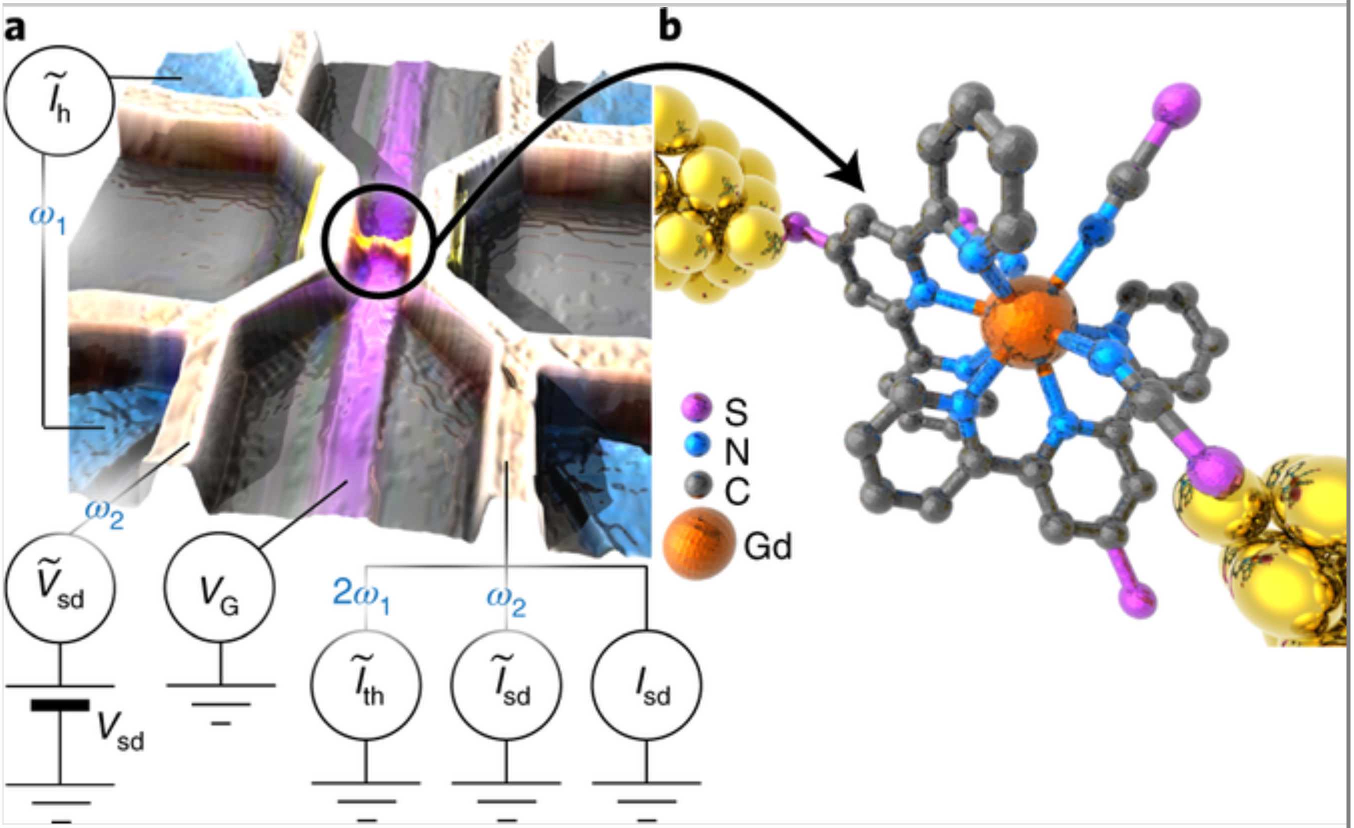

The d.c. current I_{sd}, G and $\tilde{I}_{th}$ are measured simultaneously by using a lock-in double-modulation technique in which the response to $\Delta\tilde{T}$ can be decoupled from the response to the electrical biases, so that the pure $\tilde{I}_{th}$ is accessible for any V_{sd} and V_G (Fig. 1a and Methods). These values, together with the value of $\Delta\tilde{T}$ (obtained from calibration measurements and fitting, see Methods), are then used to extract the Seebeck coefficient $S = -\tilde{V}_{th}/\Delta\tilde{T} = -\tilde{I}_{th}/\Delta\tilde{T}/(\tilde{I}_{sd}/\tilde{V}_{sd})$ for any V_{sd} and V_G. The power factor $S^2G = (\tilde{I}_{th}/\Delta\tilde{T})^2/(\tilde{I}_{sd}/\tilde{V}_{sd})$ is a direct measure of the heat-to-energy conversion efficiency in single-molecule devices.[14]

Figure 2 shows the maps of G, I_{sd} and $\tilde{I}_{th}$ as a function of V_{sd} and V_G at a cryostat temperature of $T_{base} = 2$ K. I_{sd} reveals two regions with suppressed current (due to Coulomb blockade) separated by an hourglass-shaped region of sequential electron tunnelling (Fig. 2a). This is a well-known and often-observed phenomenon in molecular junctions. In all of our junctions only one charge transition could be observed within the experimentally accessible V_G range. In the G map we can furthermore identify a line, starting from the left edge of the sequential tunnelling region at an energy of ~2 meV, that runs parallel to the right edge and corresponds to an excited molecular state (Fig. 2b). A similar excitation has been found in three other junctions (Supplementary Sections 4 and 5). Furthermore, we observe that these excited state lines do not split, shift or change in width when an 8 T magnetic field is applied, as would be expected for a spin(-multiplet) excitation of the Gd(III) centre or spin excitations of the ligand orbital. On the contrary, a handful of low-frequency intramolecular vibrational modes match this energy scale (Supplementary Section 9.2), and we thus attribute the observed lines not to spin but to vibrational excitations.

Fig. 2

Maps of electronic and thermoelectric properties.

a–**c**, Maps of d.c. current (**a**), differential conductance (**b**) and thermocurrent of a Gd-tpy junction (**c**) measured simultaneously as a function of bias and back gate voltage. The data in **b** and **c** are used to calculate the Seebeck coefficient (**d**) and the power factor (**e**) as a function of bias and back gate voltage. *N* and *N* − 1 denote the number of electrons on the molecule in the respective Coulomb blockade regions.

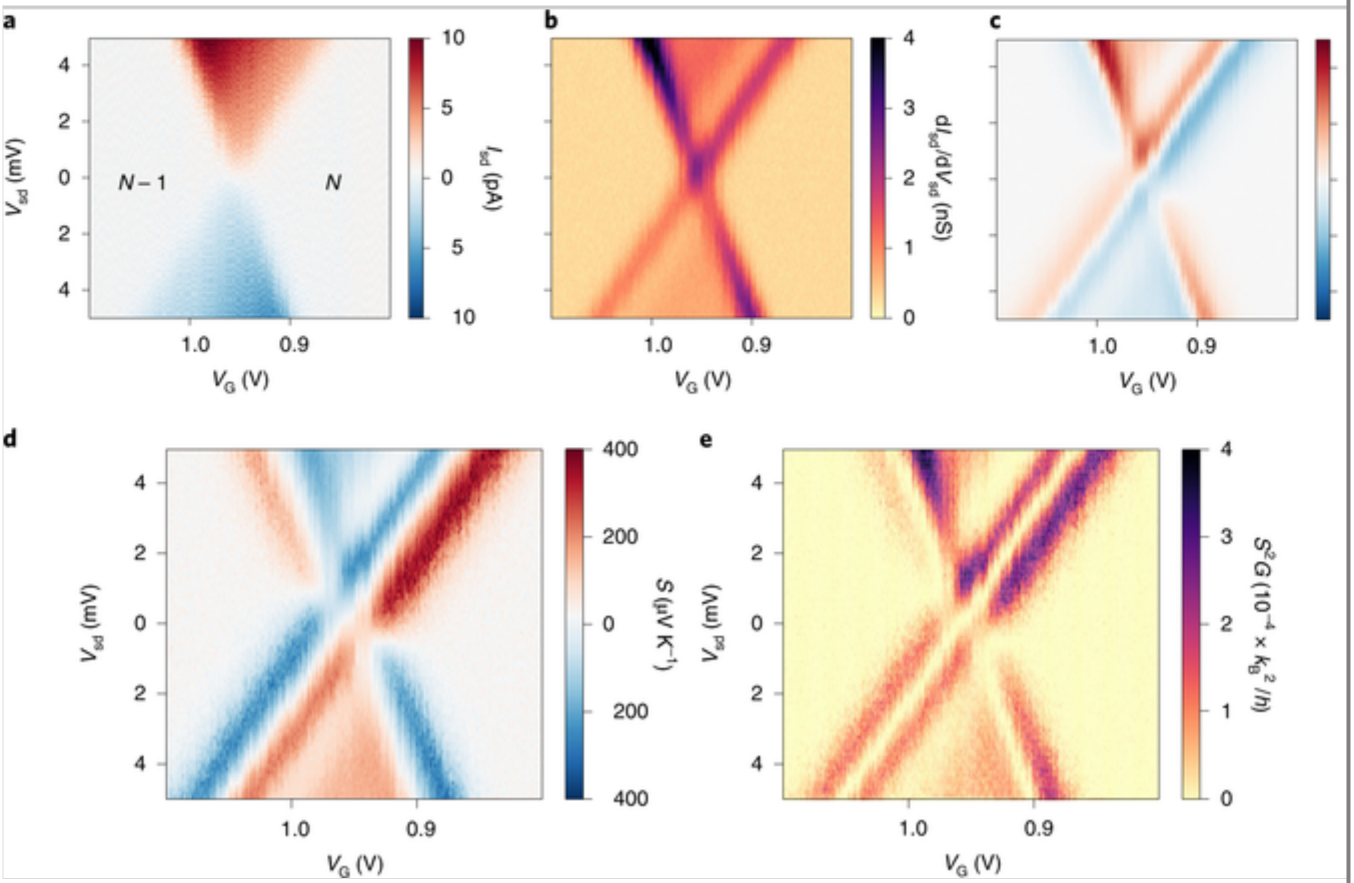

AQ8

$\tilde{I}_{th}$ displays nodes at the Coulomb diamond edges, when the chemical potential of the molecular level μ_{mol} is equal to that of the source or drain (μ_L and μ_R, with $V_{sd} = (\mu_R - \mu_L)/e$)) and reaches maximum values close to these energies (red/blue lines in Fig. 2c). The sign of the signal indicates whether the thermocurrent is carried by electrons ($I_{th} > 0$) or holes ($I_{th} < 0$). The ratio of the thermocurrent signals close to the Coulomb diamond edge with positive and negative slopes is used to estimate the temperatures of the contacts in direct vicinity of the single molecule. From a fit to our data ($\mathrm{RE}^{\mathrm{full}}$ approach, Supplementary Section 2) we find $\Delta\tilde{T} = 0.8\,\mathrm{K}$ with $T_R = 2.7$ K, $T_L = 3.5$ K, that is, T_R increases by 0.7 K. Inside the SET region we observe a non-zero value of thermocurrent (0.1 pA for $|V_{sd}| > 2$ mV), which is solely carried by the excited state (the a.c. thermoelectric response is mostly sensitive to the part of the transmission function within about $k_B T_L$ around μ_L). This is fundamentally different from I_{sd}, where the total current includes contributions by the ground and the excited states. Importantly, we note a negative–positive asymmetry of I_{th} versus V_G at points where I_{th} changes sign. This asymmetry can be clearly observed in the zero-bias trace in Fig. 3c, where $|I_{\mathrm{th,min}}/I_{\mathrm{th,max}}| = 1.4 \pm 0.2$ is found (see Supplementary Section 8 for a statistical analysis). The origin of this asymmetry is a change in spin entropy of the molecule upon adding an extra electron to it, as will be discussed below.

Fig. 3

Comparison to theoretical model.

a, I_{sd}–V_{sd} curve on resonance at $V_G = -0.96$ V. **b**, Gate-dependent zero-bias differential conductance. **c**, Thermocurrent extracted from Fig. 2. The grey circles show the experimental data, the solid lines show fits using a single-level Landauer approach (orange), a rate equation approach including spin entropy (green) and a rate equation approach including spin entropy and a vibrational mode (blue). The purple dotted lines in **c** indicate $I_{\mathrm{th,max}}$. Calculated differential conductance (**d**) and thermocurrent (**e**) as a function of bias and gate voltage using the rate equation approach including spin entropy and a vibrational mode, and the parameters extracted from the fit in **a**.

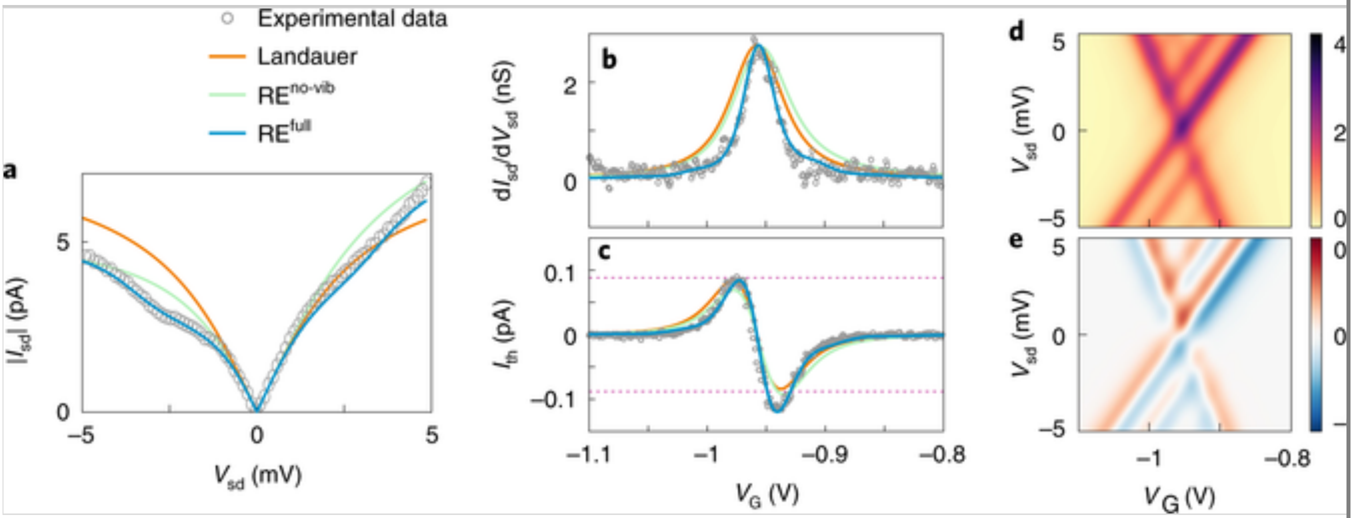

AQ9

We can now extract the Seebeck coefficient S, that is, the magnitude of the induced thermoelectric voltage in response to the temperature difference $\Delta\tilde{T} = 0.8\,\mathrm{K}$ across the single molecule, and the associated power factor S^2G (Fig. 2d,e). S changes sign when the conditions $\mu_{\mathrm{mol}} = \mu_{\mathrm{L}}$ or $\mu_{\mathrm{mol}} = \mu_{\mathrm{R}}$ are met, like $\tilde{I}_{\mathrm{th}}$, and reaches a maximum of 414 μV K^{-1} at $V_{\mathrm{sd}} = 3.4$ mV and $V_{\mathrm{G}} = -0.86$ V. An overall maximum of $S^2G = 3.6 \times 10^{-4} k_{\mathrm{B}}^2/h$ is found, where the maximum thermal response coefficient $L = \tilde{I}_{\mathrm{th}}/\Delta\tilde{T} = 0.6\,\mathrm{pA\,K^{-1}}$ is also recorded, at $V_{\mathrm{sd}} = 4.9$ mV and $V_{\mathrm{G}} = -0.99$ V. At zero bias voltage, S^2G reaches a maximum of $1.0 \times 10^{-4} k_{\mathrm{B}}^2/h$.

These data offer valuable insight into the processes at play within the molecular junction. Having access to the full V_{G}- and V_{sd}-dependent maps of I_{sd}, G and $\tilde{I}_{\mathrm{th}}$ of the single molecule, we can apply universal models (RE$^{\mathrm{full}}$ (ref. [15]), RE$^{\text{no-vib}}$, Landauer; see below and Supplementary Section 2) to reproduce $I_{\mathrm{sd}}(V_{\mathrm{sd}})$, $G(V_{\mathrm{G}})$ and $\tilde{I}_{\mathrm{th}}(V_{\mathrm{G}})$ simultaneously. To this end, the I_{sd}–V_{sd} characteristics at resonance ($V_{\mathrm{G}} = -0.96$ V) in Fig. 3a and the gate-dependent differential conductance and thermocurrent data ($V_{\mathrm{sd}} = 0$) show excellent agreement only with a rate-equation approach (RE$^{\mathrm{full}}$), where we assume that the observed excited state is of vibrational character (as suggested by the lack of any magnetic field response) and include the electronic degeneracies of the states (Supplementary Section 2). Conversely, neither the Landauer nor a rate-equation approach that ignores the vibrational excitation (RE$^{\text{no-vib}}$) are able to reproduce the data. Here the most important discrepancy between theory and experiment is the lack of negative–positive asymmetry in the Landauer model as observed in the experimental thermocurrent (Fig. 3c). The Landauer approach fails to explain this asymmetry, relying exclusively on ground-state transitions and neglecting degeneracies and electron–electron interactions. We find that asymmetric molecule-led coupling (as is found in all measured samples) is by itself insufficient to reproduce the asymmetry in the thermocurrent. Rather, the key ingredient required to model this asymmetry is the degeneracy, that is, the spin entropies, of the charge states involved in the sequential tunnelling process (Supplementary Section 13) as well as the electron–electron interactions. For I_{th}, the current-limiting step is the electron transfer to and from the 'hot' contact. Depending on the value of V_{G}, the electron transfer at the 'hot' interface corresponds either to an $N-1 \rightarrow N$ or to an $N \rightarrow N-1$ transition. As we will demonstrate below, the $N-1$ state is twofold degenerate, and the latter transition is therefore more likely than the former. This leads to the observed asymmetry of I_{th} which can thus also be present in the case of symmetric molecule-led coupling.

The rate-equation model RE$^{\mathrm{full}}$ further yields excellent agreement with the thermocurrent experimental data for $T_{\mathrm{R}} = 2.7$ K and $T_{\mathrm{L}} = 3.5$ K, and these temperatures can reproduce the full conductance and thermocurrent maps (Fig. 3d,e). The maximum calculated power factors of $0.57 \times 10^{-4} k_{\mathrm{B}}^2/h$ at zero bias and $4.3 \times 10^{-4} k_{\mathrm{B}}^2/h$ for $V_{\mathrm{sd}} = 4.9$ mV and $V_{\mathrm{G}} = -0.84$ V agree well with the $1.0 \times 10^{-4} k_{\mathrm{B}}^2/h$ and $3.6 \times 10^{-4} k_{\mathrm{B}}^2/h$ values found experimentally.

We infer that the origin of the asymmetry of I_{th} versus V_{G} (which is captured by the RE$^{\mathrm{full}}$ model) stems from the difference in the degeneracies, d_N and d_{N-1}, of the N and $N-1$

states.[11, 16] This difference in degeneracy can only arise from spin entropy.[17, 18, 19] A singlet-to-doublet transition is necessary for the fitting, when going from $N-1$ ($d_{N-1}=2$) to N ($d_N=1$) electrons. The spin entropy is given by $\mathcal{S}_N = k_\mathrm{B}\ln(d_N)$ and the resulting change is $\Delta\mathcal{S} = \mathcal{S}_{N-1} - \mathcal{S}_N = k_\mathrm{B}\ln 2$. As $\mathcal{S}_N$ contributes to the total energy of the molecule, a shift of the effective electrochemical potential μ_mol should occur with T:[20, 21]

$$\frac{\partial\mu}{\partial T} = \frac{1}{2}\Delta\mathcal{S}_{N-1\to N}\,. \qquad 1$$

The conductance peak shifts with increasing T (Fig. 4a) by a quantity $\Delta V_{\mathrm{G}_\mathrm{peak}}(T) = \Delta\mu_\mathrm{mol}\alpha$ that is connected to the capacitive couplings to the leads (C_L, C_R) and to the gate (C_G) by a proportionality factor $\alpha = (C_\mathrm{L} + C_\mathrm{R} + C_\mathrm{G})/C_\mathrm{G}$. μ_mol, extracted by fitting the conductance peaks to a single-level model[1], indeed shows a linear increase with T, with slope a of $\frac{1}{2}k_\mathrm{B}\ln 2$ (Fig. 4b). This observation agrees perfectly with what is predicted for a singlet-to-doublet transition.

Fig. 4

Temperature dependence of the differential conductance.

a, $\mathrm{d}I_\mathrm{sd}/\mathrm{d}V_\mathrm{sd}$ as a function of V_G for different temperatures. **b**, Conductance peak position as a function of temperature extracted from **a**. The purple line shows a fit to the data assuming a change of entropy of $\Delta\mathcal{S}_{N-1\to N} = k_\mathrm{B}\ln 2$. The sign of $\Delta\mathcal{S}_{N-1\to N}$ is such that for more negative gate voltages (to the left of the Coulomb peak) an empty orbital, and for less negative gate voltages (to the right of the Coulomb peak) a single occupied orbital is available for transport. The orange dotted line shows a fit assuming a change of entropy of $\Delta\mathcal{S}_{N-1\to N} = k_\mathrm{B}\ln 14 - k_\mathrm{B}\ln 2$.

AQ10

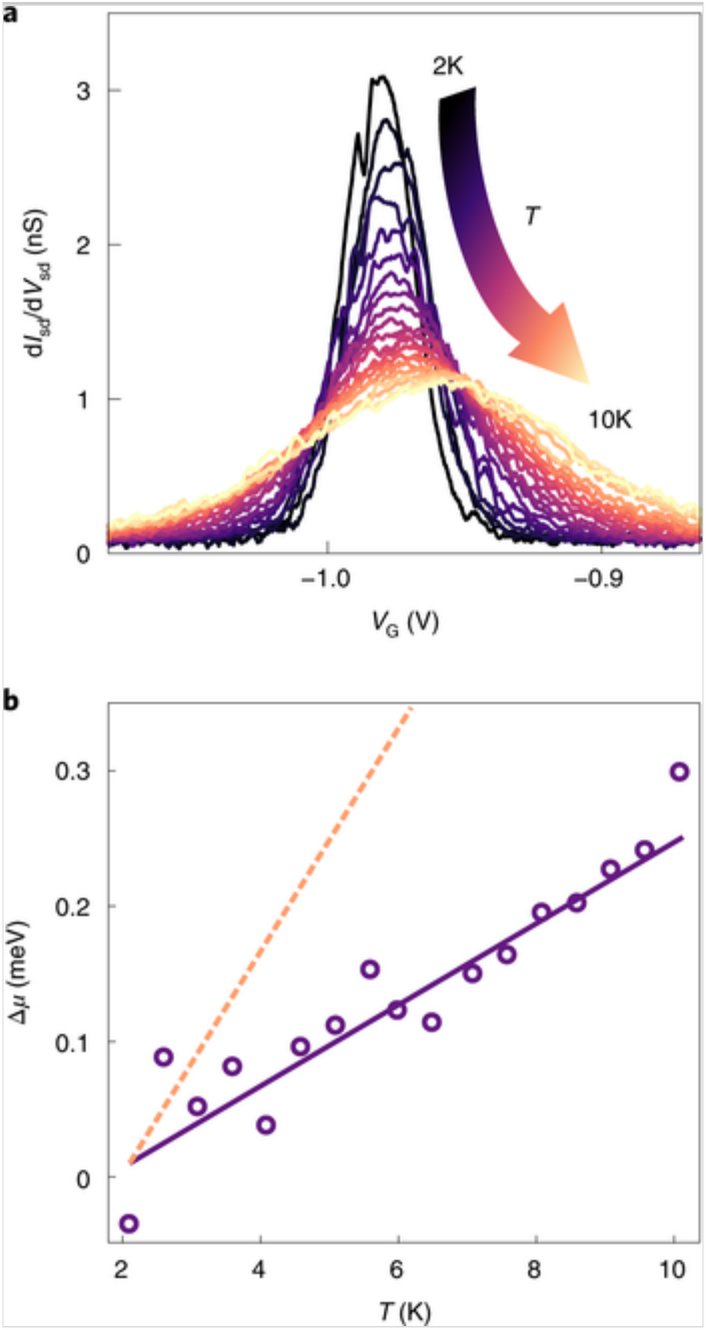

These findings provide details about the charging process of Gd-tpy: the spin-ground state of the neutral molecule is governed by the *f* orbitals of the Gd(III) centre, with $^8S_{7/2}$ and spin $\Sigma = 7/2$. If the addition or removal of the charge involved an *f*-orbital electron of the Gd centre, an entropy change of $\Delta\mathcal{S}_{N-1\to N} = k_\mathrm{B}\ln 14 - k_\mathrm{B}\ln 2$ (or $\Delta\mathcal{S}_{N\to N+1} = k_\mathrm{B}\ln 2 - k_\mathrm{B}\ln 14$) would be expected, that is, three times higher than the observed value (Fig. 4b). This indicates that the transport electron is localized on the ligands more than on the metal centre and that 4*f* electrons play a minor role (see Supplementary Sections 9.1 and 14). Furthermore, were the exchange coupling between the ligand electron and Gd higher than $k_\mathrm{B}T$, a reduction in entropy change to $\Delta\mathcal{S}_{N\to N+1} = 0$ would be expected, contrary to the experimental findings.

These results demonstrate how spin entropy determines the single-molecule thermoelectric properties. Furthermore, the Seebeck coefficient obtained here, 414 μV K^{-1}, is more than ten times higher than typical values found for conductive single-molecule devices[2, 12, 22] and close to the value found for insulating devices[23]. This illustrates that high values of S can be achieved by creating sharp features in the transmission spectrum of the junction (which in our case is achieved by weak tunnel coupling to the leads) and by bringing the Fermi energy of the leads into the vicinity of these sharp features by electrostatic gating or doping of the molecule. We nonetheless note here that weak molecule-led coupling results in low electric conductance and thus reduced power factors S^2G. This leaves ample room for further improvement: the power factors found in this study are four orders of magnitude smaller than the theoretical maximum of approximately $0.46 \times k_B^2/h$ (for a single non-interacting level).[10] Much higher values are expected by achieving symmetric coupling and by improving the coupling strengths, so that $\Gamma \approx k_B T$ and S^2G is not limited by low conductance values. Furthermore, our work indicates that molecular magnets with high changes of orbital or spin entropy upon charging can boost the efficiency of thermoelectric junctions: highly degenerate states offer multiple channels for charge transport, which boosts G without altering S. In addition, spin-entropy effects will shift the maximum conductance (Fig. 4a), leading to an increased overlap between the maxima in $S(V_G)$ and $G(V_G)$ and thus an enhancement of S^2G.

Nevertheless, we can use the experimental S^2G to estimate the thermoelectric figure of merit $ZT = S^2GT/(\kappa_{el} + \kappa_{ph})$. Our molecular junction operates in a regime where $k_BT < \hbar\omega$ with ω being the lowest-frequency vibrational mode (see Supplementary Section 9.2). Therefore—and unlike for room-temperature devices[24]—we disregard κ_{ph}, the phononic contribution to the thermal conductance. κ_{el} is then estimated by a rate equation approach that includes both spin-degeneracy and vibrational coupling (Supplementary Sections 10 and 11) and we find a $ZT \approx 0.7$ at zero bias. Our experiments further demonstrate a substantially more efficient thermoelectric heat-to-energy conversion at $T = 2$ K than at higher T (Supplementary Section 12), and highlight the need for a better theoretical understanding of the processes in play at cryogenic conditions.

AQ11

This work reveals that full thermocurrent spectroscopy is possible and can be used to directly probe single-molecule ground and excited states. It further suggests methods to maximize thermoelectric efficiency by molecular design, in ways that are not immediately available in inorganic quantum-dots, for example, by employing the symmetry-produced degeneracies of fullerenes.[25, 26] The possibility of extracting the spin entropy of a molecular junction opens the path to a plethora of effects, including magneto-cooling effects of Gd-based molecular compounds[27], spin-crossover complexes[28] or ground-state spin-blockade systems such as polyoxometalates.[29] Furthermore, our measurement protocol should make it possible to study how thermoelectric properties are influenced by Kondo correlations in single molecules in the intermediate-coupling regime.[30]

Methods

Lock-in double-modulation technique

I_{sd}, G and $\tilde{I}_{\mathrm{th}}$ are measured simultaneously. This is achieved by superimposing onto V_{sd} a small-amplitude (100 μV) a.c. voltage, $\tilde{V}_{\mathrm{sd}}$, at a frequency ω_2. The current response to ground, $\tilde{I}_{\mathrm{sd}}$, at frequency ω_2 is then used to calculate the differential conductance $G = \tilde{I}_{\mathrm{sd}}/\tilde{V}_{\mathrm{sd}}$. At the same time an a.c. heater current $\tilde{I}_{\mathrm{h}}$ at frequency $\omega_1 \ll \omega_2$ (3 and 13 Hz hereinafter) is used to create an a.c. temperature bias $\Delta\tilde{T} \propto \tilde{I}_{\mathrm{h}}^2$ at a frequency of $2\omega_1$. The current response at $2\omega_1$ is then equal to the thermocurrent $\tilde{I}_{\mathrm{th}}$. $\Delta\tilde{T}$ is calibrated by scanning thermal microscopy, by a resistance-thermometer method that uses the contacts as thermometers and by Coulomb blockade thermometry (Supplementary Section 7). Lastly, the averaged current to ground is directly measured, which yields $\tilde{I}_{\mathrm{sd}}$.

Molecular deposition

Gd-tpy molecules were deposited by immersing the sample in a 0.5 mM molecular solution in dichloromethane after electromigration and self-breaking of the gold contacts[13]. The molecule consists of a single Gd^{3+} ion ($^8\mathrm{S}_{7/2}$, S = 7/2, L = 0, g = 2) coordinated by three monodentate thiocyanate (NCS) ligands, bonded through the nitrogen and two tridentate terpy groups (terpy = 2,2′:6′,2″-terpyridine) bound through six nitrogen atoms. Each terpy group is functionalized with a single thiol anchor group. Here Gd(III) is a very stable oxidation state, with redox potentials much higher than those of the ligands. The tpy ligand is chosen to maintain structural elements of the Co-tpy complexes investigated for single-molecule transport and gives a relatively high yield of devices with junction formation; the thiocyanate SCN^- ligands are used to counterbalance the metal charge, thereby obtaining a neutral compound and completing the rare-earth coordination shell. Gd-tpy can thus couple to the gold electrodes via the thiol anchor group of the tpy or via the SCN ligand.

We performed electromigration and molecular deposition on 71 junctions and found evidence for trapping of single molecules in 11 cases (that is, a molecular junction formation yield of 15%). The remaining 60 junctions (85%) show ‘open’ behaviour where currents below the detection limit of about 10 fA for bias voltages up to 100 meV are found. These include junctions where no molecule successfully coupled to the electromigrated nano-gap after molecular deposition, junctions that failed during sample handling and those with no detectable current within the considered bias-gate window. (Typically, the Fermi energy of the leads lies deep inside the HOMO–LUMO gap of the molecule. Asymmetric coupling and the associated image charge corrections to the level alignment may help to bring one of the frontier levels closer to the Fermi energy of the leads, making a charge transition accessible within the gate window used.)

Theoretical analysis

The first step in the theoretical analysis was a fit of the resonant I–V characteristics (at $V_G = -0.96$ V) to the three theoretical models used, described in detail in Supplementary Sections 2 and 3. Briefly, we used the Landauer model which describes transport through a single non-degenerate and non-interacting level; the $RE^{\text{no-vib}}$ rate-equation model which includes the electronic degeneracy of one of the charge states; and the RE^{vib} model which includes both the degeneracy of one of the charge states and electron-vibrational coupling (in this case to a single vibrational level). The results of the I–V fits are shown in Fig. 3a, and the parameters extracted from the fits are given in Supplementary Table I. Those parameters were then used to calculate the zero-bias conductance plotted in Fig. 3b. To describe the zero-bias thermocurrent, we once again use the parameters from the I–V fits and perform another fitting with T_L and T_R as fitting parameters. Only the RE^{vib} model provided an adequate fit as shown in Fig. 3c. The resulting electrode temperatures T_L and T_R were then used in the subsequent calculations.

Online content

Any methods, additional references, Nature Research reporting summaries, source data, extended data, supplementary information, acknowledgements, peer review information; details of author contributions and competing interests; and statements of data and code availability are available at https://doi.org/10.1038/s41565-021-00859-7.

Supplementary information

The online version contains supplementary material available at https://doi.org/10.1038/s41565-021-00859-7.

Peer review information *Nature Nanotechnology* thanks the anonymous reviewers for their contribution to the peer review of this work.

Acknowledgements

We acknowledge financial support from the EU (Marie-Skłodowska-Curie 748642-TherSpinMol and 707252-SpinReMag; ERC-StG-338258-OptoQMol, ERC-CoG-773048-MMGNRs, FET-767187-QuIET); the Glasstone Research Fellowship; the Royal Society (URF and grant funds) and the Royal Society of Edinburgh; the EPSRC (EP/T01377X/1, EP/N017188/1-QuEEN, EP/R513295/1-Doctoral Prize); and the NWO/OCW (Frontiers of Nanoscience programme and Vrij Programma-CISS). We acknowledge use of the University of Oxford Advanced Research Computing facility (https://doi.org/10.5281/zenodo.22558) and the Quest high-performance computing facility at Northwestern University, jointly supported by the Office of the Provost, the Office for Research and Northwestern University Information Technology.

Author contributions

P.G. conceived the project and performed the electrical/thermoelectric measurements. P.G. and J.K.S. evaluated the data and performed the fitting. J.K.S. developed the theoretical transport models supervised by E.M.G. J.d.B. and C.H. supported the experiments. M.v.d.S. fabricated the devices. J.J.L.R. and L.B. synthesized the compound. The manuscript was written through contributions of all authors. All authors have given approval to the final version of the manuscript.

AQ15

Data availability

Data for the main text are available online at https://doi.org/10.4121/13264931. Any other supporting data can be made available upon request to the corresponding author.

Competing interests The authors declare no competing interests.

Supplementary information

Supplementary Information

Supplementary Figs. 1–13, Sections 1–14 and Tables I–III.

References

1. Gehring, P., Thijssen, J. M. & van der Zant, H. S. J. Single-molecule quantum-transport phenomena in break junctions. *Nat. Rev. Phys.* **1**, 381–396 (2019).

2. Park, S., Kang, H. & Yoon, H. J. Structure–thermopower relationships in molecular thermoelectrics. *J. Mater. Chem. A* **7**, 14419–14446 (2019).

3. Koch, J., von Oppen, F., Oreg, Y. & Sela, E. Thermopower of single-molecule devices. *Phys. Rev. B* **70**, 195107 (2004).

4. Lambert, C. J., Sadeghi, H. & Al-Galiby, Q. H. Quantum-interference-enhanced thermoelectricity in single molecules and molecular films. *C. R. Phys.* **17**, 1084–1095 (2016).

5. Murphy, P., Mukerjee, S. & Moore, J. Optimal thermoelectric figure of merit of a

molecular junction. *Phys. Rev. B* **78**, 161406 (2008).

6. Agarwalla, B. K., Jiang, J.-H. & Segal, D. Thermoelectricity in molecular junctions with harmonic and anharmonic modes. *Beilstein J. Nanotechnol.* **6**, 2129–2139 (2015).

7. Park, S., Kang, S. & Yoon, H. J. Power factor of one molecule thick films and length dependence. *ACS Cent. Sci.* **5**, 1975–1982 (2019).

8. Widawsky, J. R., Darancet, P., Neaton, J. B. & Venkataraman, L. Simultaneous determination of conductance and thermopower of single molecule junctions. *Nano Lett.* **12**, 354–358 (2012).

9. Kim, Y., Jeong, W., Kim, K., Lee, W. & Reddy, P. Electrostatic control of thermoelectricity in molecular junctions. *Nat. Nanotechnol.* **9**, 881–885 (2014).

10. Gehring, P. et al. Field-effect control of graphene–fullerene thermoelectric nanodevices. *Nano Lett.* **17**, 7055–7061 (2017).

11. Harzheim, A. et al. Role of metallic leads and electronic degeneracies in thermoelectric power generation in quantum dots. *Phys. Rev. Res.* **2**, 013140 (2020).

12. Rincón-García, L., Evangeli, C., Rubio-Bollinger, G. & Agraït, N. Thermopower measurements in molecular junctions. *Chem. Soc. Rev.* **45**, 4285–4306 (2016).

13. O’Neill, K., Osorio, E. A. & van der Zant, H. S. J. Self-breaking in planar few-atom au constrictions for nanometer-spaced electrodes. *Appl. Phys. Lett.* **90**, 133109 (2007).

14. Behnia, K. *Fundamentals of Thermoelectricity* (Oxford University Press, 2019).

15. Sowa, J. K., Mol, J. A., Briggs, G. A. D. & Gauger, E. M. Beyond Marcus theory and the Landauer–Büttiker approach in molecular junctions: a unified framework. *J. Chem. Phys.* **149**, 154112 (2018).

16. Josefsson, M. et al. A quantum-dot heat engine operating close to the thermodynamic efficiency limits. *Nat. Nanotechnol.* **13**, 920–924 (2018).

17. Kleeorin, Y. et al. How to measure the entropy of a mesoscopic system via thermoelectric transport. *Nat. Commun.* **10**, 5801 (2019).
AQ16

18. Viola, G., Das, S., Grosfeld, E. & Stern, A. Thermoelectric probe for neutral edge modes in the fractional quantum hall regime. *Phys. Rev. Lett.* **109**, 146801 (2012).

19. Mazal, Y., Meir, Y. & Dubi, Y. Nonmonotonic thermoelectric currents and energy harvesting in interacting double quantum dots. *Phys. Rev. B* **99**, 075433 (2019).

20. Beenakker, C. Theory of Coulomb-blockade oscillations in the conductance of a quantum dot. *Phys. Rev. B* **44**, 1646 (1991).

21. Hartman, N. et al. Direct entropy measurement in a mesoscopic quantum system. *Nat. Phys.* **14**, 1083–1086 (2018).

22. Cui, L., Miao, R., Jiang, C., Meyhofer, E. & Reddy, P. Perspective: thermal and thermoelectric transport in molecular junctions. *J. Chem. Phys.* **146**, 092201 (2017).

23. Garner, M. H. et al. Comprehensive suppression of single-molecule conductance using destructive σ-interference. *Nature* **558**, 415–419 (2018).

24. Cui, L. et al. Thermal conductance of single-molecule junctions. *Nature* **572**, 628–633 (2019).

25. Ke, S.-H., Baranger, H. U. & Yang, W. Addition energies of fullerenes and carbon nanotubes as quantum dots: the role of symmetry. *Phys. Rev. Lett.* **91**, 116803 (2003).

26. Sowa, J. K., Mol, J. A. & Gauger, E. M. Marcus theory of thermoelectricity in molecular junctions. *J. Phys. Chem. C.* **123**, 4103–4108 (2019).

27. Evangelisti, M. et al. Cryogenic magnetocaloric effect in a ferromagnetic molecular dimer. *Angew. Chem. Int. Ed.* **50**, 6606–6609 (2011).

28. Dugay, J. et al. Phase transitions in spin-crossover thin films probed by graphene transport measurements. *Nano Lett.* **17**, 186–193 (2017).

29. de Bruijckere, J. et al. Ground-state spin blockade in a single-molecule junction. *Phys. Rev. Lett.* **122**, 197701 (2019).

30. Costi, T. A. Magnetic field dependence of the thermopower of Kondo-correlated quantum dots. *Phys. Rev. B* **100**, 161106 (2019).